



Research paper

A novel revolute joint of variable stiffness with reconfigurability



Zhongyi Li, Shaoping Bai*

Department of Materials and Production, Aalborg University, Aalborg 9220, Denmark

ARTICLE INFO

Article history:

Received 17 September 2018

Revised 25 November 2018

Accepted 10 December 2018

Available online 21 December 2018

Keywords:

Variable stiffness mechanism

Reconfigurable mechanism

Multi-mode stiffness variation

Exoskeletons

ABSTRACT

In this paper, a novel revolute joint of variable stiffness with reconfigurability (JVS_R) is presented. The JVS_R is designed with a compliant joint mechanism, and is able to vary widely its stiffness in multiple modes, namely, linear, hardening and softening modes. This brings the joint for many potential applications in novel transmission and robotics. In the paper, mathematical models of joint stiffness are developed for the JVS_R, with which influences of design parameters are analyzed. A prototype of JVS_R is constructed and preliminary test results validate the model. A design case is included to illustrate the application of the JVS_R in exoskeletons.

© 2018 Elsevier Ltd. All rights reserved.

1. Introduction

Robotic joints with inherent compliance can find applications in rehabilitation robots [1–5], wearable exoskeletons [6–9], legged robots [10–12] and service robots [13–15]. In general, the compliant joints are used for increasing safe physical human–robot interaction (pHRI) or improving the dynamical adaptability with environment, as well as enhancing the energy efficiency. Up to date, many compliant joints exhibiting different stiffness performance have been proposed. They can be classified into two types: the joints of fixed compliance and the adjustable compliance joints [1].

The fixed compliance type joints usually utilize linear springs in series with stiff actuators. The series elastic actuator (SEA) is the most famous example in this type. A rotary SEA presented in [7] was designed to actuate an orthosis. A helical torsion spring with constant stiffness is installed between a DC motor and a human joint to enhance pHRI safety. The device was used as a torque generator as well as a torque sensor in robotic systems, thus a desired control performance was achieved. Another fixed compliance joint with a customized torsion spring is presented in [6]. Safe human–robot interaction and torque estimation were achieved by integrating the joint into a knee orthosis. In [11,16,17], energy efficiency with fixed compliance joint was investigated. The study shows that, due to the constant stiffness, the energy efficiency of the robotic device is generally low and can only be improved when the trajectory behavior of robotic joint matches the natural frequency of the system. Moreover, SEA using linear spring experiences another limitation that the design needs to tradeoff between system bandwidth and torque resolution [18,19]. As an alternative, fixed compliance joints with nonlinear behaviors have been developed in recent years, considering that nonlinear behavior offers more design parameters than a linear one and more flexible in shaping stiffness/torque-deflection profiles. In [19], a nonlinear SEA with hardening stiffness behavior

* Corresponding author.

E-mail addresses: shb@mp.aau.dk, shb@m-tech.aau.dk (S. Bai).

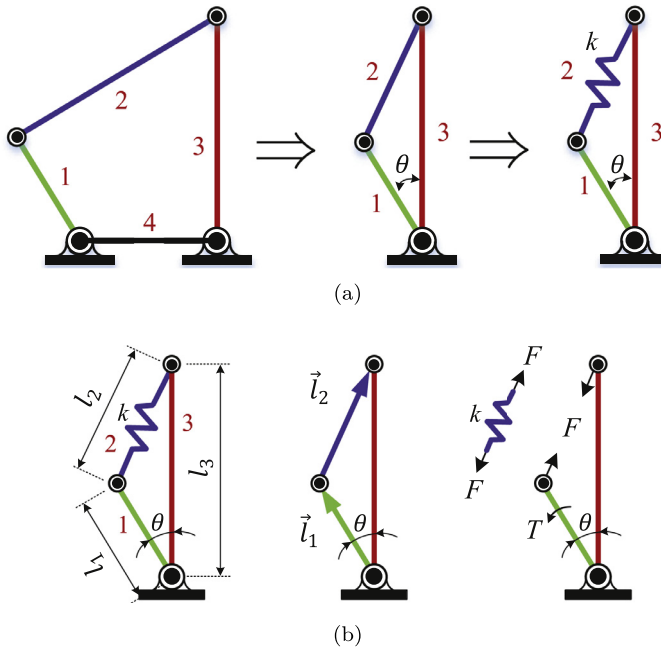


Fig. 1. (a) The concept of constructing a compliant joint by utilizing a special case of four-bar linkage. (b) Kinematic and static diagram of the mechanism.

was proposed to overcome the limitation of the design tradeoff, which can maintain a higher torque resolution at low deflection and a larger response bandwidth for high deflection. In [20], Park et al. designed a joint mechanism with softening stiffness behavior which can maintain high stiffness for a low external force, but reduce stiffness for a large external load, hence guaranteeing both position accuracy and collision safety.

Contrary to the fixed compliance type joint, the adjustable compliance joints are able to change their stiffness dynamically. They can be designed with different principles, such as spring preload based principle [3,12,21–23], transmission ratio based principle [24–29], and special springs [30,31]. Ham et al. [12] proposed the MACCEPA where stiffness variation is achieved by adjusting the preload of a spring. The VS-joint [23] is another design based on spring preload principle where a cam disk of a specific shape is used to change the preload. Other adjustable compliance devices, such as AwAS [26,27], MeRIA [28], MESTRAN [29], VSJ [30], VSA-CubeBot [32] and CompactAct-VSA [33] are noticeable too. However, in most cases of adjustable compliant joints a secondary motor is usually used to actively tune an elastic element to achieve stiffness variation. As a consequence, the adaptable compliant joint is heavy and complex.

It is noticed that the existing designs, both fixed compliance and adjustable compliance joints, show limitations in achieving nonlinear stiffness behavior. Only a few devices [19,23,34–36] are able to adjust stiffness performance achieving multiple behaviors. In the design in [34], a hypocycloid mechanism was used to stretch a spring with linear stiffness in a nonlinear way. The mechanism can achieve approximate linear and hardening behaviors, excluding softening behavior. In [19,23,35,36], different behaviors were achieved by redesigning cam shape, with which design parameters of the mechanism need to be adjusted. Some studies show that nonlinear stiffness behavior is helpful in improving energy efficiency [18], collision safety [20] and stability [37]. Thus new designs that are able to adjust stiffness behavior are desirable for improving compliant joint performance.

In this paper, a novel revolute joint of variable stiffness with reconfigurability is proposed. The new design attempts to achieve a variable stiffness with multiple modes and to ease the adjustment of stiffness. The idea of the compliant joint mechanism design is shown in Fig. 1. Through the adjustment of the design preload, the variable stiffness can be achieved, and three working modes showing hardening, softening and linear behaviors can be realized. Moreover, a reconfigurable design based on the mechanism is proposed to effectively facilitate the adjustment of its stiffness and output-torque ranges. The proposed mechanism is novel in its capacities of reconfiguration and variable stiffness adjustment together with a compact architecture.

The paper is organized as follows: Section 2 describes basic concept of stiffness variation based on a compliant joint mechanism and conducts the associated stiffness analysis. The design of JVSR is presented in Section 3, followed by the stiffness modeling. In Section 4, a prototype of JVSR and its test-rig are constructed, with which experiments are carried out to validate the ability of stiffness adjustment of JVSR. In Section 5, a case study is described in which the proposed mechanism is scaled for joints of an upper-body exoskeleton. Section 6 concludes this work.

2. Basic concept of stiffness variation

2.1. Kinematic principle

The JVSR can be treated as a special case of the four bar linkage. For a four-bar rigid-body linkage, the speed ratio between the crank and the follower, a.k.a. mechanical advantage, is the function of link lengths and rotation angle, so is the torque ratio. In a special case when the length of the ground link is zero, the torque ratio, or the reciprocal of the speed ratio, becomes a constant of 1. The linkage becomes singular when the three links are collinear. If we replace one rigid link with elastic element, the stiffness at the singular configuration is zero.

[Fig. 1](#) shows the kinematic principle of the new design of joint with variable stiffness. By replacing the coupler, bar-2, with compliant material (e.g. spring, rubber, or thin metal strips) of stiffness k , a compliant joint mechanism is obtained.

2.2. Stiffness model

To facilitate the modeling, we assume that the bar-1 is the input link, while bar-3 is the output link. The angle between the output and the input links is denoted by θ . Furthermore, the input and the output links (bar-1 and 3) are considered as rigid and articulated with the base by pin joints. Let the lengths of bar-1, 2 and 3 be l_1 , l_2 and l_3 respectively, which satisfy the constraint

$$l_2^2 = l_1^2 + l_3^2 - 2l_1l_3 \cos\theta. \quad (1)$$

Moreover, let F and T be the tension along bar-2 and the external equilibrium torque applied on the joint, respectively, then

$$T = F \cdot \left| \hat{l}_2 \times \vec{l}_1 \right| = J \cdot F, \quad (2)$$

where \hat{l}_2 is the unit vector of \vec{l}_2 , and $J = \left| \hat{l}_2 \times \vec{l}_1 \right| = \frac{\partial l_2}{\partial \theta} \in \mathbb{R}^1$ is the linkage Jacobian, which is a scalar for the mechanism.

The equivalent rotational stiffness of output link, $K_{eq} \in \mathbb{R}^1$, represents a linear relationship between the infinitesimal torque δT and the infinitesimal deflection $\delta\theta$, which is described by:

$$\delta T = K_{eq} \cdot \delta\theta. \quad (3)$$

Combining [Eq. \(3\)](#) together with [Eq. \(2\)](#), and given that $\delta F = k \cdot \delta l_2$, K_{eq} can be obtained as:

$$K_{eq} = \frac{\delta T}{\delta\theta} = J \cdot \frac{\delta F}{\delta\theta} + \frac{\delta J}{\delta\theta} \cdot F. \quad (4)$$

That is,

$$K_{eq} = J \cdot k \cdot J + \frac{\delta J}{\delta\theta} \cdot F = J^2 k + \frac{\delta J}{\delta\theta} \cdot F. \quad (5)$$

The stiffness K_{eq} in [Eq. \(5\)](#) is composed of two terms, $J^2 k$ and $\frac{\delta J}{\delta\theta} \cdot F$, which are contributed by the stiffness of compliant coupler k and the internal tension F respectively. According to Hooke's law, the internal tension F is given by

$$F = k \cdot (l_2 - l_{2,0}) + k \cdot (l_{2,0} - l_{2,r}) = k \cdot \delta l_2 + F_0, \quad (6)$$

where $l_{2,0}$ represents the length of bar-2 when $\theta = 0$, and $l_{2,r}$ is the free length of elastic element, and F_0 is the pretension of elastic element for $\theta = 0$.

Substituting [Eq. \(6\)](#) into [Eq. \(5\)](#) and rearranging it, we get the equivalent stiffness K_{eq} associated with the initial tension F_0

$$K_{eq} = \underbrace{J^2 k + \frac{\delta J}{\delta\theta} \cdot k \cdot \delta l_2}_{K_{eq,1}} + \underbrace{\frac{\delta J}{\delta\theta} \cdot F_0}_{K_{eq,2}}, \quad (7)$$

where $K_{eq,1}$ and $K_{eq,2}$ are the stiffness induced by the stiffness of compliant coupler k and the pretension F_0 respectively.

We introduce a length ratio $\lambda = l_1/l_3$, ($\lambda \in (0, 1)$) and substituting it into [Eq. \(7\)](#) gives

$$K_{eq} = kl_3^2 \hat{K}_{eq,1}(\lambda, \theta) + F_0 l_3 \hat{K}_{eq,2}(\lambda, \theta), \quad (8)$$

where

$$\hat{K}_{eq,1}(\lambda, \theta) = \frac{K_{eq,1}}{k \cdot l_3^2} = \hat{J}^2 + \frac{\delta \hat{J}}{\delta\theta} \cdot \delta \hat{l}_2, \quad (9)$$

$$\hat{K}_{eq,2}(\lambda, \theta) = \frac{K_{eq,2}}{F_0 \cdot l_3} = \frac{\delta \hat{J}}{\delta\theta}, \quad (10)$$

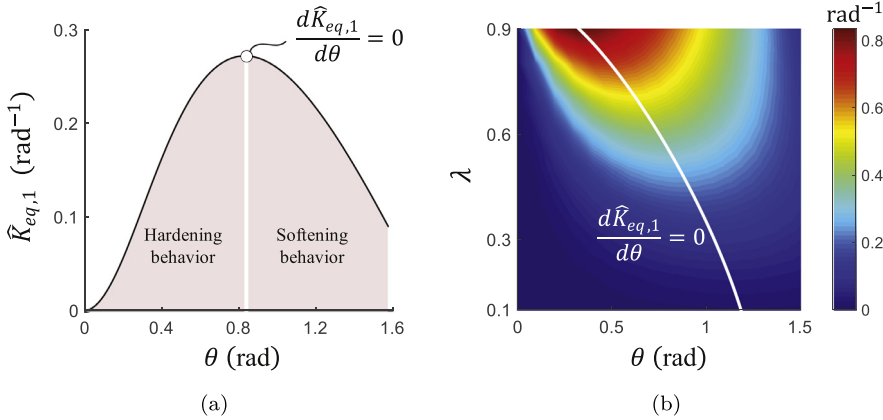


Fig. 2. Stiffness performance of $\hat{K}_{eq,1}$. (a) Stiffness $\hat{K}_{eq,1}$ as a function of the deflection angle θ with $\lambda = 0.5$. (b) Influence of $\lambda = l_1/l_3$ on $\hat{K}_{eq,1}$.

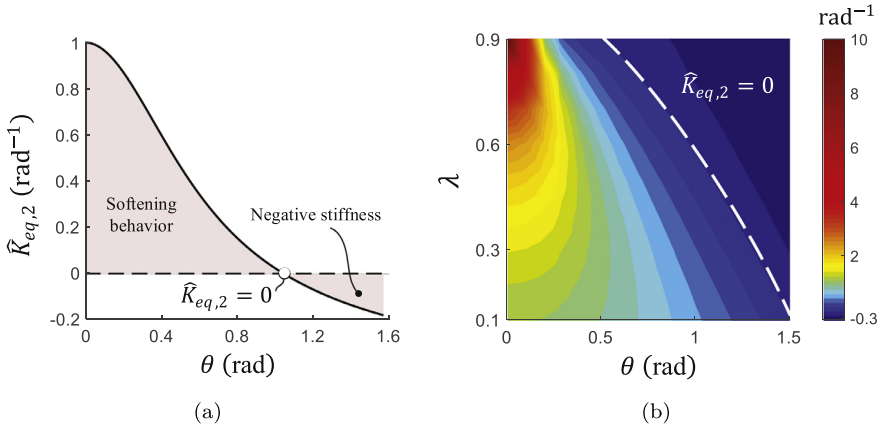


Fig. 3. Stiffness performance of $\hat{K}_{eq,2}$. (a) Stiffness $\hat{K}_{eq,2}$ as a function of the deflection angle θ with $\lambda = 0.5$. (b) Influence of $\lambda = l_1/l_3$ on $\hat{K}_{eq,2}$.

with $\hat{f} = \lambda \sin \theta / \hat{l}_2$ and $\hat{l}_2 = \sqrt{\lambda^2 - 2\lambda \cos \theta + 1}$. Note that $\hat{K}_{eq,1}$ and $\hat{K}_{eq,2}$ in Eqs. (9) and (10) are related only to the parameters of λ and θ . In other words, they are factors that are influenced only by mechanism geometry. We herein investigate the properties of $\hat{K}_{eq,1}$ and $\hat{K}_{eq,2}$, and look at the influences on the stiffness performance.

As $\hat{K}_{eq,1}$ and $\hat{K}_{eq,2}$ change with respect to the joint deflection θ and the design parameter λ , we look into the influence of each parameter. Fig. 2 shows the change of $\hat{K}_{eq,1}$ with respect to θ , and the influence of λ . As can be seen from Fig. 2(a), the stiffness curve in the range $[0, \pi/2]$ rad can be divided into two intervals, separated at the deflection angle $\theta \mid_{d\hat{K}_{eq,1}/d\theta=0}$. The separation line divides the entire curve into two intervals of different behaviors, namely, hardening behavior and softening behavior. Joint stiffness hardening means an increase in the equivalent stiffness, while softening is the opposite, i.e., a reduction in the equivalent stiffness.

Two special points in Fig. 2(a) should be noted. One is $\theta = 0$ where the configuration stands for a singular point, thus the joint shows zero stiffness. The other is $\theta \mid_{d\hat{K}_{eq,1}/d\theta=0}$ which is described as the position where the rate of the torque increase of $Jk \cdot \delta l_2$ is maximum as θ increases within $[0, \pi/2]$ rad. Through adjusting the ratio $\lambda = l_1/l_3$, different stiffness performances can be achieved as shown in Fig. 2(b). In this figure, the white line of $d\hat{K}_{eq,1}/d\theta = 0$ represents all maximum $\hat{K}_{eq,1}$ for any given ratio λ . We can also see that a larger λ will yield a smaller range of intervals for hardening behavior but a larger maximum value of $\hat{K}_{eq,1}$.

Fig. 3 shows the change of stiffness $\hat{K}_{eq,2}$ in the range $[0, \pi/2]$ rad. As can be seen in Fig. 3(a), the $\hat{K}_{eq,2}$ monotonically decreases as θ increases. Moreover, it shows a softening behavior first. After $\hat{K}_{eq,2}$ reaches zero at $\theta \mid_{\delta f/\delta\theta=0}$, it shows a negative stiffness. Referring to Eq. (2), the special point, $\theta \mid_{\delta f/\delta\theta=0}$, stands for the position where \vec{l}_1 and \vec{l}_2 are vertical. Fig. 3(b) shows the influence of the ratio $\lambda = l_1/l_3$ on $\hat{K}_{eq,2}$. We can see that a larger λ will yield a smaller range of intervals for softening behavior but a larger value of $\hat{K}_{eq,2}$ at $\theta = 0$.

Eq. (8) indicates that F_0 affects the overall stiffness by scaling $\hat{K}_{eq,2}$ which can be observed from Fig. 4 showing the changes of K_{eq} . In Fig. 4, the solid line $\frac{dK_{eq}}{d\theta} = 0$ and dash line $K_{eq} = 0$ separate the whole region into three parts. They

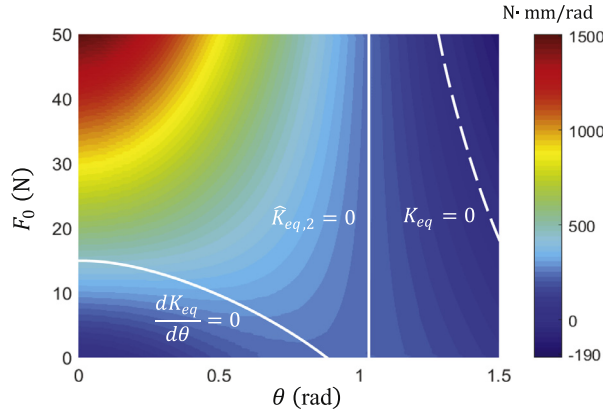


Fig. 4. The distribution of the equivalent stiffness K_{eq} for varying deflection angle θ and the initial tension F_0 with $\lambda = 0.5$, $k = 1$ N/mm and $l_3 = 30$ mm.

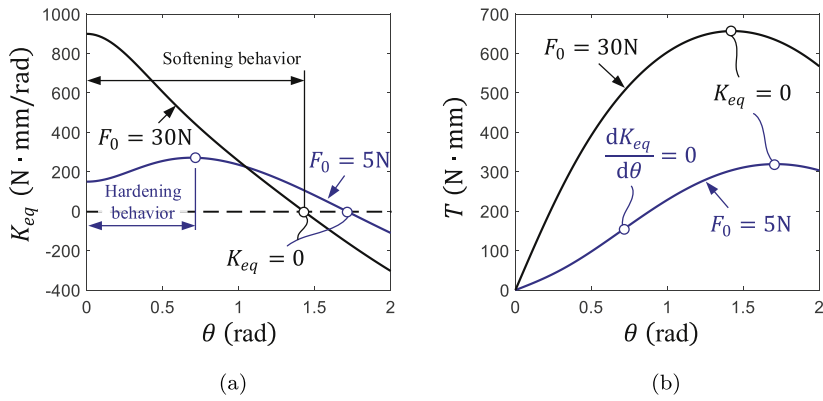


Fig. 5. (a) Stiffness curves and (b) the corresponding torque curves for different pretensions, in which other parameters are assigned as $\lambda = 0.5$, $k = 1$ N/mm and $l_3 = 30$ mm.

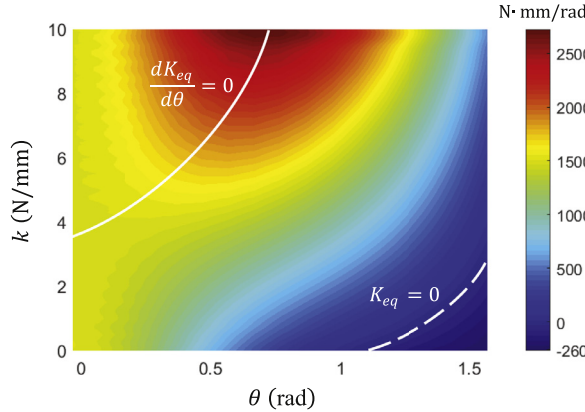


Fig. 6. The variation of the equivalent stiffness K_{eq} for varying deflection angle θ and the stiffness k with $F_0 = 50$ N, $\lambda = 0.5$ and $l_3 = 30$ mm.

correspond to the hardening behavior area (in the lower-left corner), the softening behavior area and the negative stiffness area (in the higher-right corner). Moreover, recalling that $\hat{K}_{eq,1}$ at singular point ($\theta = 0$) is zero, the joint stiffness is therefore solely determined by $K_{eq,2}$. In Fig. 4, the stiffness variation at point of $\theta = 0$ for changing F_0 can be observed clearly.

Fig. 5 shows two cases with $F_0 = 5$ N and $F_0 = 30$ N to illustrate further the influence of F_0 . The stiffness and torque curves are displayed in Fig. 5(a) and 5(b). In Fig. 5(a), both hardening and softening behaviors can be observed from the curves, showing the influence of pretension F_0 on stiffness performance of the mechanism.

Eq. (8) also indicates that the stiffness k influences the stiffness performance by scaling $\hat{K}_{eq,2}$. Fig. 6 shows the change of stiffness with respect to θ and k .

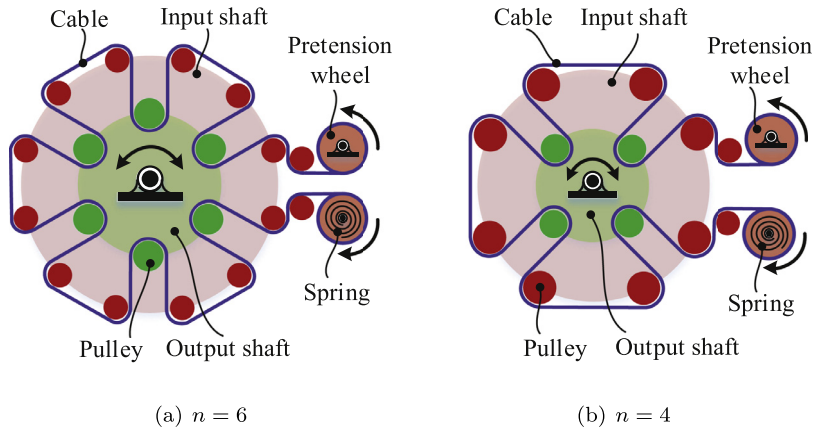


Fig. 7. Schematic design of JVSR, (a) an example design with $n = 6$, (b) another example design with $n = 4$.

It is noted that the negative stiffness mentioned represents a decreasing equilibrium torque when deflection is increased. Taking the case for $F_0 = 30\text{ N}$ in Fig. 5 as an example, the compliant joint mechanism shows negative stiffness when the deflection angle exceeds $\theta = 1.45\text{ rad}$. At this point, the torque due to the spring force reaches the maximum and then starts to reduce when the deflection angle increases. The calculated equivalent stiffness thus becomes negative.

3. Development of JVSR

3.1. Design of JVSR

Based on the aforementioned variation stiffness principle, a reconfigurable compliant revolute joint mechanism is proposed as shown in Fig. 7. In this mechanism, the compliant joint mechanism is implemented as a cable wrapped on three pins (pulleys), one in the output link and the other two in the input link. The mechanism design is reconfigurable by wrapping the cable around different number of pins. In the design, the number of pins on the input shaft are two times of the number of pins in the output shaft. Herein, we use the number of pins on the output link, n , to describe the reconfigured design. Fig. 7(a) and 7(b) show two reconfigurations, $n = 6$ and $n = 4$. In the mechanism, two coaxial shafts, input shaft and output shaft, are coupled through the cable. One end of the cable is reeled, while the other end of the cable is connected to a linear spring of stiffness k with pretension F_0 .

With the new design, reconfiguration is feasible not only by changing the number of pins, but also by pattern of wrapping. Fig. 8 illustrates the reconfiguration of JVSR with $n = 6$. It can be seen that six configurations can be implemented by different cable wrapping. In this light, we use one more number N ($N \leq n$) to indicate the number of branches, namely, the number of pins on the output shaft that are wrapped by cables.

3.2. Stiffness modeling of JVSR

For the sake of simplicity, the following assumptions are made for the modeling:

- The spring is the only compliant element in the system, cable and structure elements being considered rigid.
- The system is frictionless.

It should be noted that although the cable is considered as rigid, due to the stretch of the cable, the actual linear spring is replaced by an equivalent stiffness to compensate for it, as in Eq. (21).

The schematic of a single branch of JVSR is shown in Fig. 9, which is slightly different to the compliant joint mechanism in Fig. 1 due to the real construction. All major geometrical parameters, except λ , l_3 and θ illustrated in the four-bar linkage model, have been labeled in Fig. 9 and defined as follows:

- R_1 , R_2 and R_3 are the radii of pulley-1, 2 and 3 respectively, and are identical ($R_1 = R_2 = R_3 = R$).
- b is the diameter of cable.
- a is the distance between the axes of the pulley-2 and 3, which is given by

$$a = 2R_1 + R_2 + R_3 + 2b \approx 4R. \quad (11)$$

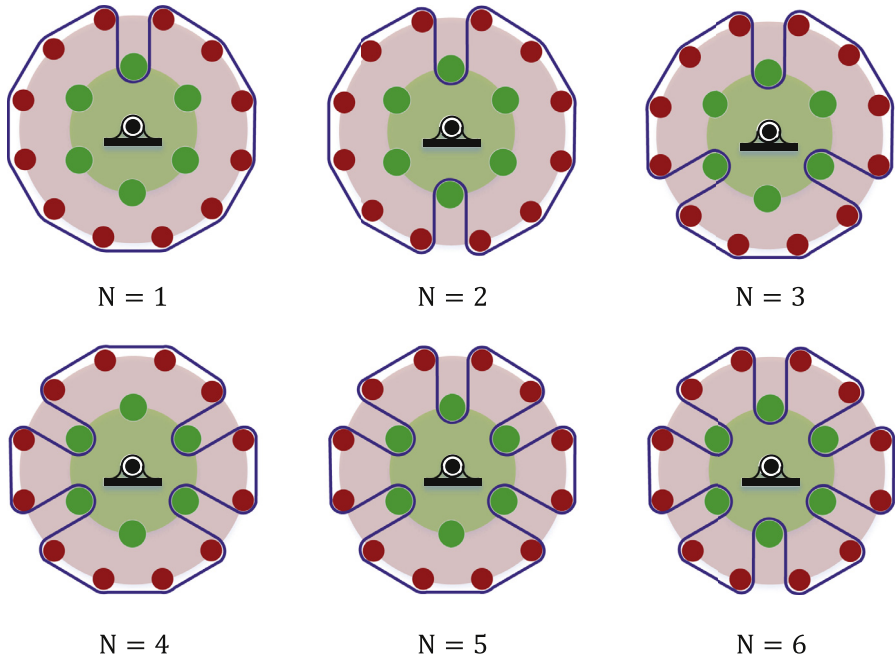


Fig. 8. Reconfiguration of JCSR ($n = 6$) indicated by the number of pins wrapped.

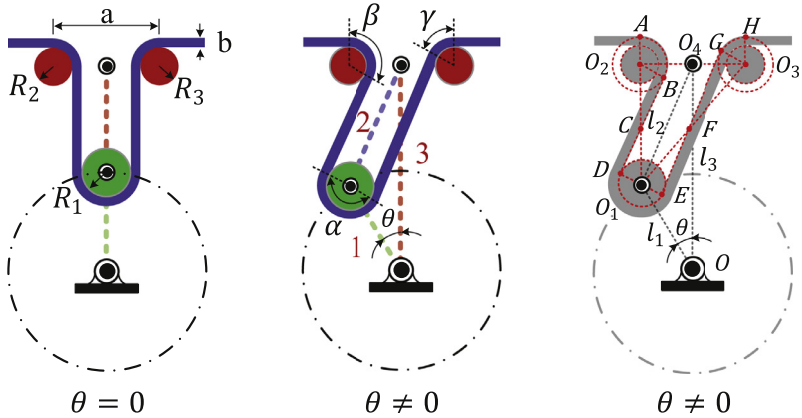


Fig. 9. The schematic of a single branch of JCSR.

- α , β and γ are the contact angles between cable and pulley-1, 2, 3 respectively, which can also be expressed as

$$\left\{ \begin{array}{l} \alpha = \beta + \gamma \\ \beta = \arccos\left(\frac{a - 2l_1 \sin \theta}{\sqrt{4l_2^2 - 4al_1 \sin \theta + a^2}}\right) - \arccos\left(\frac{a}{\sqrt{4l_2^2 - 4al_1 \sin \theta + a^2}}\right) + \frac{\pi}{2} \\ \gamma = \arccos\left(\frac{a + 2l_1 \sin \theta}{\sqrt{4l_2^2 + 4al_1 \sin \theta + a^2}}\right) - \arccos\left(\frac{a}{\sqrt{4l_2^2 + 4al_1 \sin \theta + a^2}}\right) + \frac{\pi}{2}. \end{array} \right. \quad (12)$$

In Fig. 9, the cable length is calculated as

$$l = \frac{a \cdot \alpha}{2} + |\vec{DB}| + |\vec{EG}|, \quad (13)$$

where $|\vec{DB}| = \sqrt{l_2^2 - al_1 \sin \theta}$, $|\vec{EG}| = \sqrt{l_2^2 + al_1 \sin \theta}$.

In order to distinguish from the symbols used in Section 2, we use J_1 , K , K_1 and K_2 to represent the Jacobian, the equivalent stiffness of the joint, the induced stiffness $K_{eq,1}$ and $K_{eq,2}$ respectively.

Based on the derivation of Eq. (2), the Jacobian is obtained by differentiating Eq. (13), which is given by

$$J_1 = \frac{\partial l}{\partial \theta}. \quad (14)$$

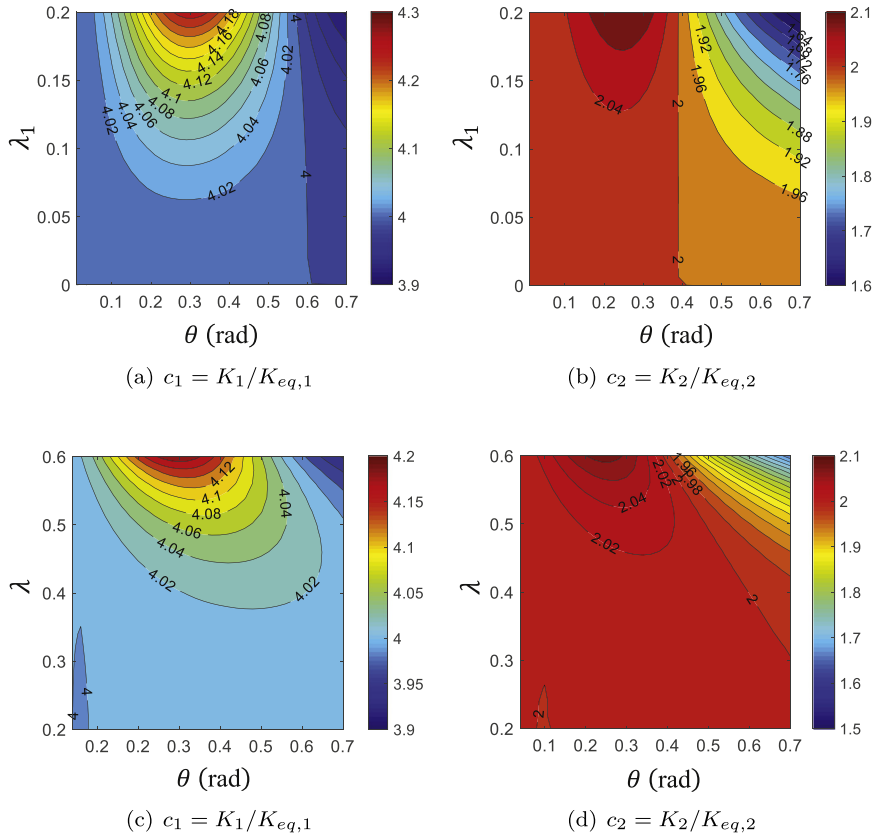


Fig. 10. Contour plots of c_1 and c_2 as a function of λ (λ_1) and θ , (a) c_1 with $\lambda = 0.6$, (b) c_2 with $\lambda = 0.6$, (c) c_1 with $\lambda_1 = 0.18$, (d) c_2 with $\lambda_1 = 0.18$.

The torque model of Eq. (2) and the stiffness model of Eq. (7) are rewritten as

$$T = J_1 \cdot F, \quad (15)$$

$$K = \underbrace{J_1 \cdot k \cdot J_1}_{K_1} + \underbrace{\frac{\delta J_1}{\delta \theta} \cdot k \cdot \delta l}_{K_2} + \underbrace{\frac{\delta J_1}{\delta \theta} \cdot F_0}_{K_3}. \quad (16)$$

The detailed expression of K is not included for clarity. So far, we have obtained the equivalent stiffness model of mechanism in Fig. 9. We define a ratio of $\lambda_1 = R/l_3$, which satisfies

$$0 < \lambda_1 < \sqrt{1 + 4\lambda_1^2} - 2\lambda_1. \quad (17)$$

Furthermore, we define $c_1 = K_1/K_{eq,1}$ and $c_2 = K_2/K_{eq,2}$ which describe the changes due to the geometry of mechanical parts, compared to the simplified model, and Eq. (16) can be rewritten as

$$K = c_1 l_3^2 k \hat{K}_{eq,1}(\lambda, \theta) + c_2 l_3 F_0 \hat{K}_{eq,2}(\lambda, \theta). \quad (18)$$

Fig. 10 shows the variations of c_1 and c_2 with respect to the changes of θ , λ and λ_1 . The figure shows that when λ and λ_1 are small, the two coefficients, c_1 and c_2 , are nearly unchanged even though the deflection angle θ increases.

If N branches are utilized in JVSR, the total stiffness of the joint becomes

$$K = N^2 c_1 l_3^2 k \cdot \hat{K}_{eq,1} + N c_2 l_3 F_0 \cdot \hat{K}_{eq,2}, \quad (19)$$

and the torque model of the JVSR becomes

$$T = N^2 k \delta l J_1 + N F_0 J_1. \quad (20)$$

This is the complete model of the JVSR, which can achieve multi-mode stiffness variation by reconfiguration and parameter adjustment. The overall working principle of stiffness variation is shown in Fig. 11.

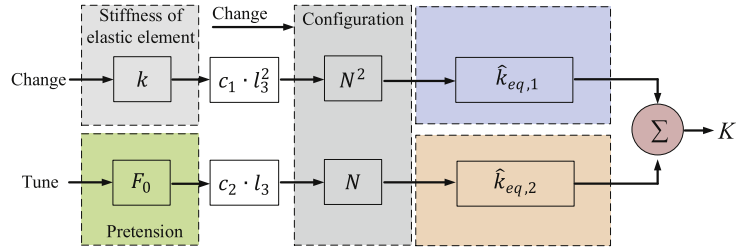


Fig. 11. The overall working principle of stiffness variation.

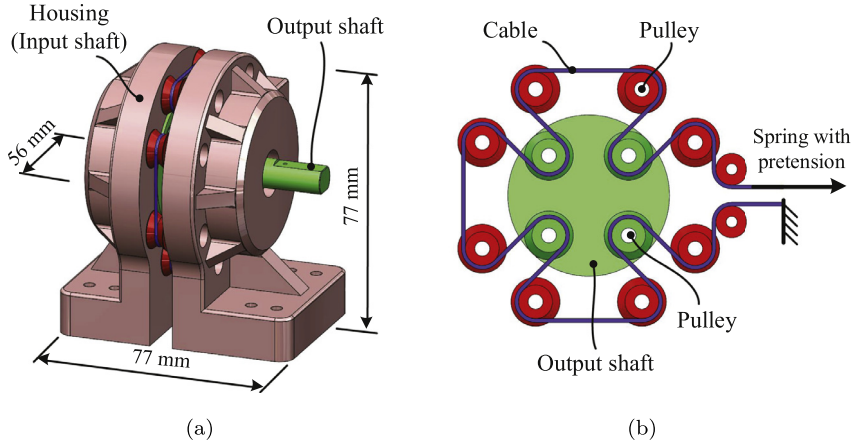


Fig. 12. JVS design for experimental test. (a) CAD Model of the JVS prototype. (b) Design of cable arrangement.

Table 1
Parameters for the JVS prototype.

Parameters	Values
Dimensions (length × width × height)	77 × 56 × 77 mm
Weight	0.268 kg
n	4
Ratio λ	0.6
Ratio λ_1	0.18
Length of bar-3, l_3	25 mm

4. Prototyping and testing

In this section, a prototype of JVS along with its test rig setup is described. Experimental results with the prototype are presented, analyzed and compared with the results from analytical simulation.

4.1. Prototype of JVS

The prototype model of JVS is shown in Fig. 12. The design is in accordance with the model described in Fig. 7(b). A total of four configurations can be obtained. In the testing, the input shaft is fixed to the housing of JVS (see Fig. 12(a)) and cannot rotate in the experiments. Thus, there is only one equilibrium position, $\theta = 0$, in this prototype. In the future design, the input shaft can be connected to a position motor, thereby, the equilibrium position and stiffness can be independently controlled. Fig. 12(b) shows the details of cable arrangement in the prototype. A nylon cable of 1 mm diameter is used in our JVS prototype, which is able to sustain for a maximum tension of about 50N. Linear spring is connected to one end of the nylon cable. The other end of the nylon cable is fixed on the housing.

The JVS prototype is able to work in both softening and hardening modes for the controllable tension limit of cable. Table 1 summarizes the main design parameters of JVS prototype. To evaluate the influence of k on the stiffness performance of JVS, two springs, spring 1 of $k_{s,1} = 0.6613\text{N/mm}$ and spring 2 of $k_{s,2} = 0.214\text{N/mm}$, were used. Simulation of stiffness variation for different pretensions and configurations of spring 1 is shown in Fig. 13. From this figure, all three modes of spring stiffness varying, namely, hardening, softening and linear modes can be observed. The solid lines in Fig. 13(a) and 13(b) differentiate hardening and softening modes. Within areas bounded by the dash lines the JVS prototype approximately exhibits constant stiffness, which can be considered as a linear spring. From Fig. 13, we also see that the

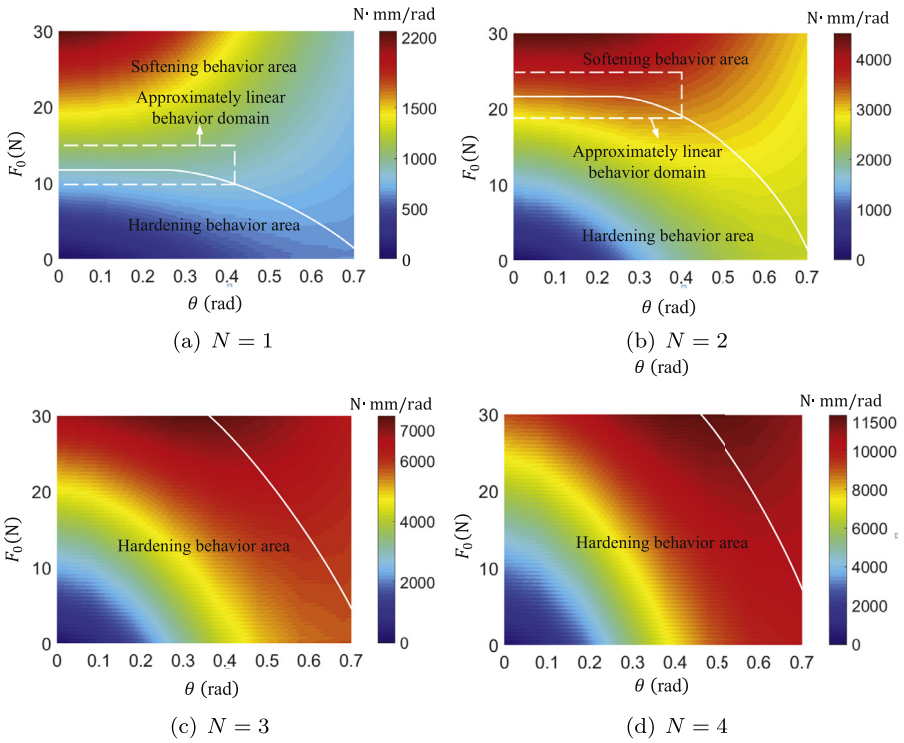


Fig. 13. Simulation of JVSР prototype stiffness v.s. cable pretension F_0 and rotation deflection of output shaft θ for different configurations, (a) $N = 1$, (b) $N = 2$, (c) $N = 3$, (d) $N = 4$.

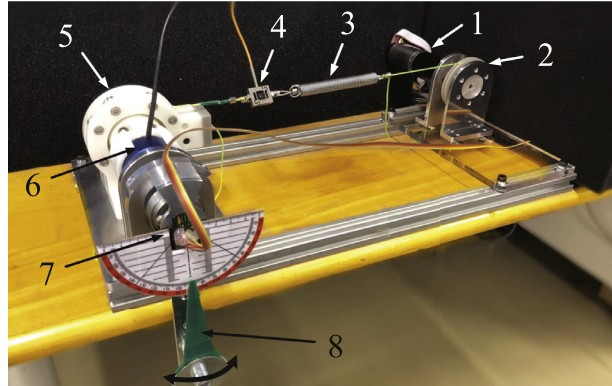


Fig. 14. JVSР test rig constructed with (1) motor-gearbox, (2) winch, (3) linear spring, (4) load cell, (5) JVSР, (6) torque sensor, (7) encoder, (8) pendulum.

area of hardening mode becomes larger with the increase of N , which is also in accordance with the expression of Eq. (19). Moreover, a larger stiffness adjustment range under the same angle deflection θ can be obtained with the increase of N .

4.2. Test rig and experiment setup

The testing setup is depicted in Fig. 14. A nylon cable is routed around a winch, which is used to adjust the cable tension in the experiments. A motor with gearbox which is installed along the winch provides an alternative to control the cable pretension automatically in this test rig. Standard linear spring is connected along the nylon cable. A load cell (model: Forsentek FS01–10 kg) is mounted between the winch and spring, and this instrument ensures a measure of force with an accuracy of 0.1N. A torque sensor (model: Forsentek FTE–20 NM) is installed along the output shaft of JVSР to measure the applied torque on the shaft with an accuracy of 0.04N·m. For the convenience of applying torque on the shaft, a pendulum is designed, and is connected to the torque sensor through the shaft. An absolute encoder (model: RLS RMB20) is used to measure the rotation angle θ of the pendulum with an accuracy of 0.5°. The sensory data is acquired with an Arduino DUE board, which is also used for motor control by working together with the ESCON motor driver.

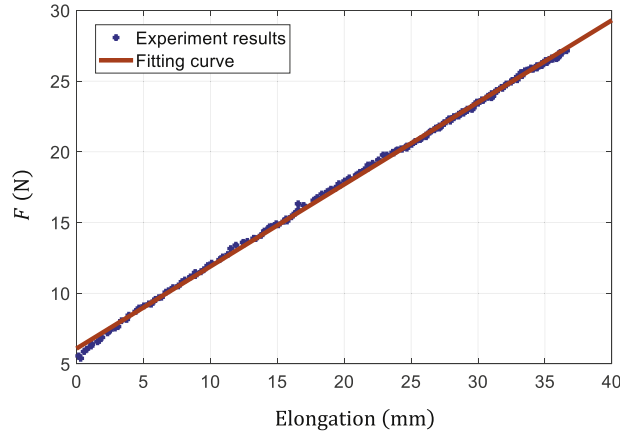


Fig. 15. The force-vs-elongation curves of the nylon cable, wherein the dots denote experiment results, and the solid line denotes the fitting curve.

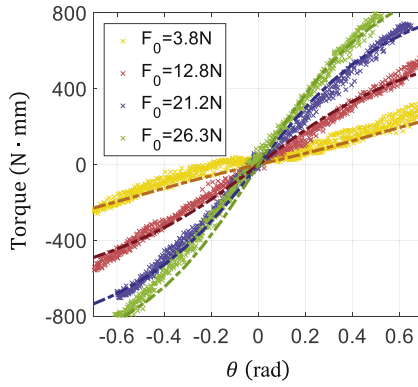


Fig. 16. Plot of torque versus deflection θ for varying pretension F_0 with $N = 1$. All dots denote experiment results, and the dash-dot lines denote simulation results.

Considering the stiffness of nylon cable k_c , and the stiffness of the linear spring k_s , the total stiffness of the cable can be found by

$$k = \frac{k_s \cdot k_c}{k_s + k_c}. \quad (21)$$

Fig. 15 shows the cable tension F that were measured and the elongation of cable calculated using Eq. (13) with deflection angle of pendulum θ . Linear curve fitting yields

$$F = 0.5804x + 6.089, \quad (22)$$

where x denotes the elongation of nylon cable. This curve fitting can achieve R-squared value of 0.9991, showing that it closely matches the experiment results. Therefore, the nylon cable stiffness k_c is 0.5804 N/mm, and the total stiffness $k_1 = 0.309\text{N/mm}$ for the use of spring 1 and the total stiffness $k_2 = 0.156\text{ N/mm}$ for the use of spring 2 are then obtained based on Eq. (21).

4.3. Experiments

Experiments were performed to assess the influences of pretension F_0 , configuration number N and spring stiffness k on the performance of stiffness. In the testing, external torque is applied on the pendulum to rotate the joint following the sequence, $0 \rightarrow 0.7 \rightarrow 0 \rightarrow -0.7 \rightarrow 0\text{rad}$, and at least four periods of this sequence are recorded for every measurement.

4.3.1. Effect of pretension F_0

During the test, four different pretensions $F_0 = 3.8\text{N}, 12.8\text{N}, 21.2\text{N}, 26.3\text{N}$ were set in the test rig for $N = 1$ and $k_1 = 0.309\text{N/mm}$. The torque-deflection relationships based on different pretensions are shown in Fig. 16. As can be seen, the simulation results indicated by the solid lines closely match the measurements of the dotted lines with maximum error $\pm 46\text{N}\cdot\text{mm}$. Different stiffness varying behaviors can also be observed clearly. The joint shows first hardening behavior at beginning with $F_0 = 3.8\text{N}$, and then transits to softening behavior with the increase of pretension, which is consistent with

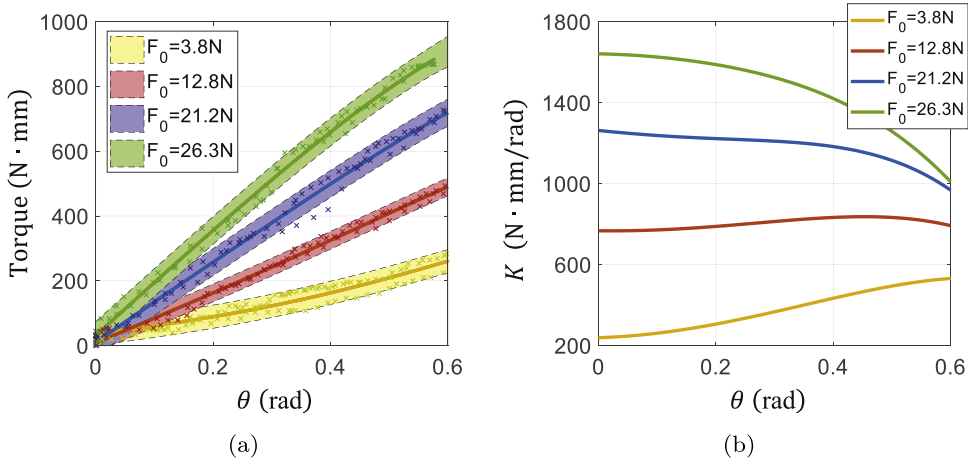


Fig. 17. (a) Plot of torque versus joint deflection θ for varying pretension F_0 , wherein the dots denote experiment results, and the solid lines denote the fitting results, and the shadow areas denote the confidence intervals. (b) Plot of joint stiffness versus deflection θ for varying pretension F_0 . $N = 1$, $k_1 = 0.309\text{N/mm}$.

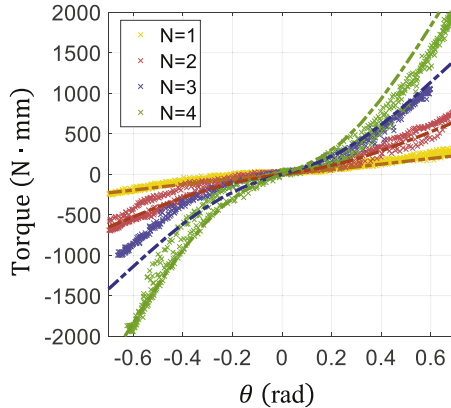


Fig. 18. Plot of torque versus deflection θ based on different configurations for $F_0 = 3.5\text{N}$, wherein the dots denote experiment results, and the dash-dot lines denote simulation results.

the analysis in Sections 2 and 3. Fig. 17(a) shows the fitted curves for the measurements, obtained with fifth-order polynomials. Fig. 17(b) shows the stiffness variation with respect to deflection obtained by derivation of the fitting curves. In both figures, we show only the results in the range of $\theta \in [0, 0.6]\text{rad}$ for clarity. The variations of stiffness behaviors with different pretension can be observed clearly.

4.3.2. Effect of configuration N

Different configurations of $N = 1, 2, 3, 4$ were set in the JVSR for $F_0 = 3.5\text{N}$ and $k_1 = 0.309\text{N/mm}$. As depicted in Fig. 18, the measured results are generally in accordance with the simulated ones with maximum error $\pm 110\text{N}\cdot\text{mm}$. In Fig. 19, the experimental results show that increasing N leads to a higher stiffness value as expressed in Eq. (19). We also see that the hardening behavior is more evident with the increase of N . That is because the weight of $\hat{K}_{eq,1}$ in Eq. (19) increases as N increases, and $\hat{K}_{eq,1}$ shows hardening behavior around the position of $\theta = 0$ as discussed in Section 2.

4.3.3. Effect of spring stiffness k

Finally, a test was performed to evaluate the influence of spring stiffness k on the performance of JVSR for the condition of $N = 4$ and $F_0 = 3\text{N}$. The test results in Fig. 20 are generally in accordance with the simulated ones, although the mechanism shows hysteresis behaviors in the experimental results, in which the maximum error is $\pm 122\text{N}\cdot\text{mm}$. Fig. 21 shows stiffness variation, wherein the influence of k on the stiffness performance can be observed clearly. As can be seen, the hardening behavior is more evident with a more stiff spring, which is in accordance with Eq. (19), where the value of the hardening behavior related term, $N^2 c_1 l_3^2 k \hat{K}_{eq,1}$, is large for a high stiffness k . Moreover, the two curves meet nearly at the same point for $\theta = 0$, which demonstrates the zero-stiffness property of $\hat{K}_{eq,1}$ at singularity of the compliant joint mechanism.

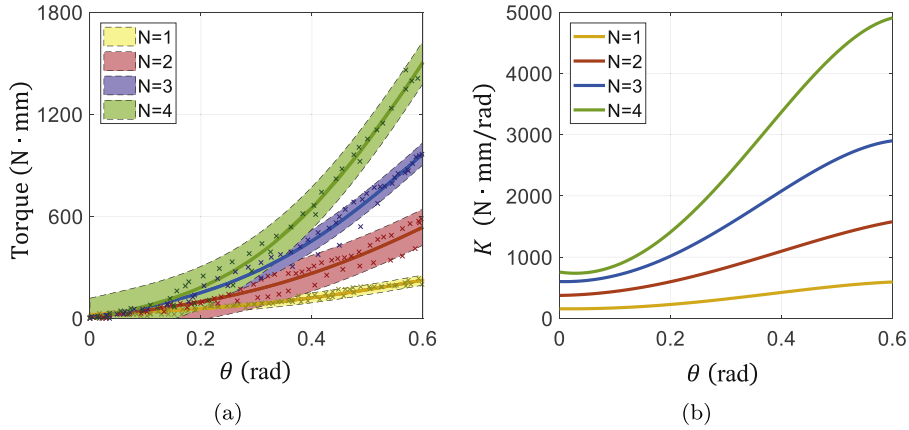


Fig. 19. (a) Plot of torque versus joint deflection θ of different configurations, wherein the dots denote experiment results, and the solid lines denote the fitting results, and the shadow areas denote the confidence intervals. (b) Plot of joint stiffness versus deflection θ for different configurations.

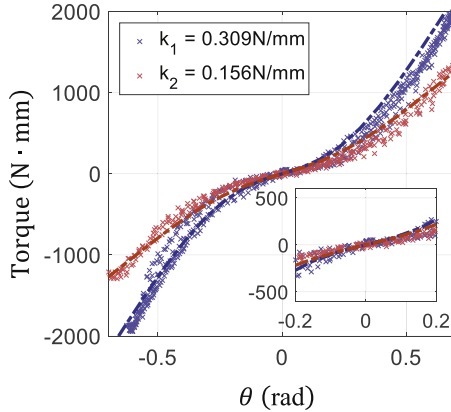


Fig. 20. Plot of torque versus deflection θ for different springs with $N = 4$ and $F_0 = 3\text{N}$, wherein the dots denote experiment results, and the dash-dot lines denote simulation results.

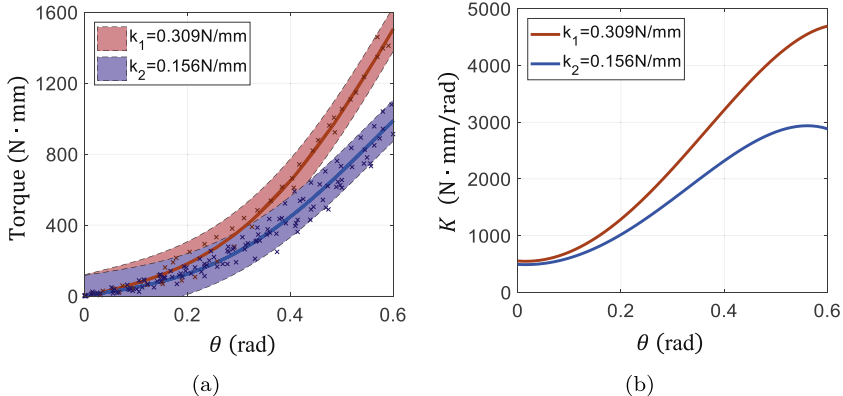


Fig. 21. (a) Plot of torque versus joint deflection θ for different springs, wherein the dots denote experiment results, and the solid lines denote the fitting results, and the shadow areas denote the confidence intervals. (b) Plot of joint stiffness versus deflection θ for springs of different stiffness.

5. A case of design

We herein include a case to illustrate how the new joint mechanism is scalable to a specific application. In the case, the application considered is the joints of an upper-body exoskeleton [38,39] as shown in Fig. 22.

In the exoskeleton, three active joints (two for shoulder joint, and one for elbow joint) are used. The torque requirements of joints are shown in Table 2. The geometric parameters of JVSR are summarized in Table 3, where N_s and N_e

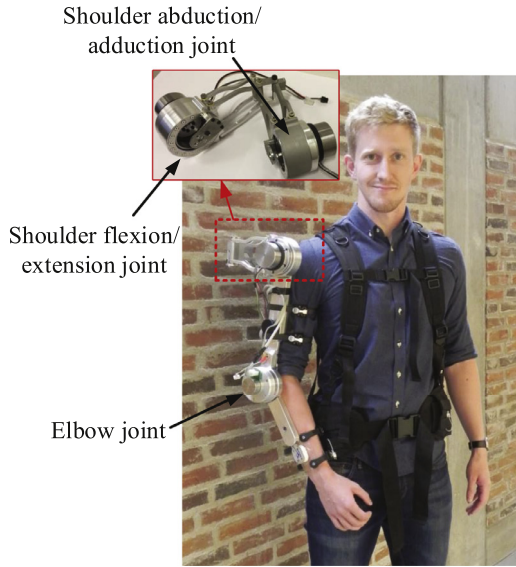


Fig. 22. An upper-body exoskeleton [38,39].

Table 2
Output torques and dimensions of the upper-body exoskeleton joints [38,39].

Joint	Related torque	Diameter
Shoulder flexion/extension	11.2 N·m	95 mm
Shoulder abduction/adduction	18 N·m	85 mm
Elbow	10 N·m	95 mm

Table 3
Parameters of the compliant actuator.

n	λ	λ_1	l_3	k	N_e	N_s
5	0.6	0.15	30 mm	2.3 N/mm	4	5

stand for the reconfiguration numbers for the shoulder abduction/adduction joint, and elbow and shoulder flexion/extension joints, respectively. Considering the maximum deflection angle in a general compliance joint [8], we define θ in the range of $[-0.45, 0.45]$ rad. According to the torque model Eq. (20) and the above defined values, and given that $F_0 = 40$ N and $T = 20$ N·m, the equivalent stiffness of elastic element can be calculated as $k \approx 2.3$ N/mm. Fig. 23 shows the functions of maximum output torque and the maximum stiffness with respect to the changes of deflection angles when different configurations are applied. We can see that in this case the JVSR with $N_s = 5$ is applicable to the shoulder abduction/adduction joint, and the JVSR with $N_e = 4$ is applicable to the shoulder flexion/extension and elbow joints.

It should be noted that the spring in the designed JVSR is selected to withstand the maximum tension,

$$F_{\max} = Nk\delta l|_{\theta=\theta_{\max}} + F_0 = 131 \text{ N}, \quad (23)$$

and the corresponding maximum tension length,

$$\Delta L_{\max} = N\delta l|_{\theta=\theta_{\max}} + \frac{F_0}{k} = 56 \text{ mm}. \quad (24)$$

The cable is selected considering its strength limitation to withstand the maximum tension. We choose a steel wire, and its cross-sectional area A satisfies [40]

$$A \geq \frac{F_{\max}}{\sigma_f} = 0.187 \text{ mm}^2, \quad (25)$$

where σ_f is the tensile strength for the steel material. A steel cable with a diameter of 0.9 mm is selected, which can withstand the maximum tension without failure. To avoid the long extension of a linear spring, a torsional spring as shown in Fig. 25 is used. The stiffness k_t of torsional spring satisfies

$$k_t = l_m^2 \cdot k_s = 230 \text{ N} \cdot \text{mm}/\text{rad}, \quad (26)$$

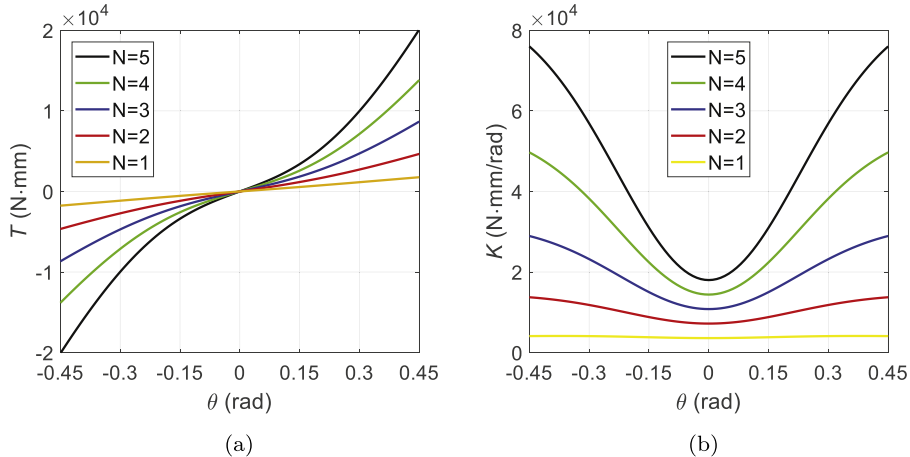


Fig. 23. Functions of (a) the maximum output-torque and (b) the maximum stiffness with respect to the changes of deflection angles for different configurations for $F_0 = 30\text{N}$.

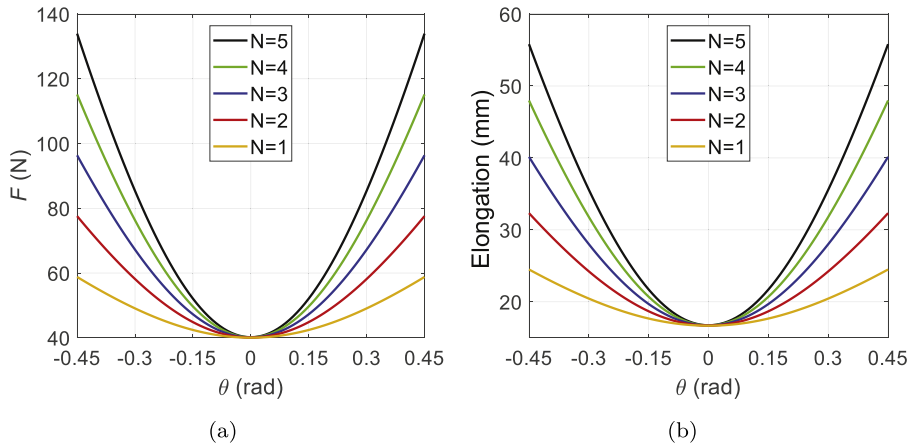


Fig. 24. The functions of (a) the spring tension and (b) the corresponding elongation length with respect to the changes of deflection angles of the JVSR with different configuration.

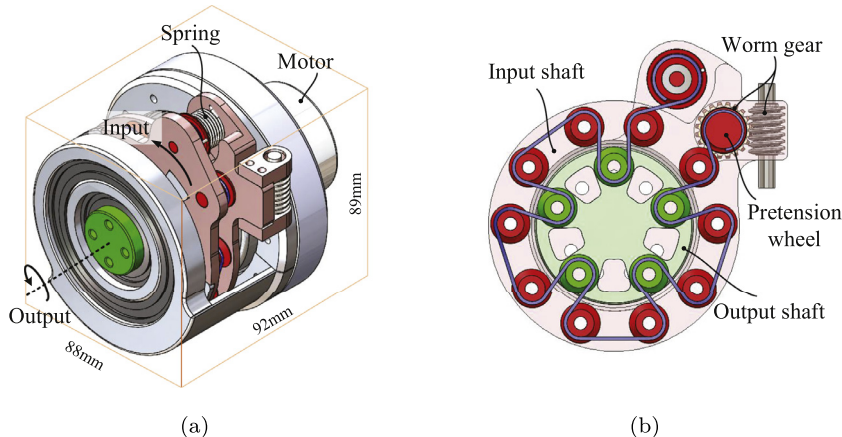


Fig. 25. An embodiment of JVSR. (a) 3D model. (b) Design of cable arrangement.

Table 4
Specifications of the steel wire and torsional spring.

Specification	Values
Material of the steel wire	304 stainless steel
Tensile strength of the cable material σ_f	700 MPa
Diameter of the wire ϕ	0.9 mm
Material of the spring	SWP-B steel
Desired maximum deflection of the spring	± 5.6 rad
Mean diameter of the spring D	20 mm
Wire diameter of the spring d	1.8 mm
Number of turns of the spring	7

where l_m is the length of moment arm, which is set to 10mm.

An embodiment of the design is shown in Fig. 25. A worm gear is used to adjust manually pretension of the cable. The specifications of the selected steel cable and torsional spring are listed in Table 4. The total mass of the designed joint is 0.987kg, including the motor.

6. Conclusions

This paper presents an innovative design of revolute joint of variable stiffness with reconfigurability (JVSR). The design of JVSR features the capabilities of adjusting initial stiffness and changing stiffness behavior within a compact architecture. In this work, a mathematical model of JVSR is developed and validated experimentally. A design case is included to illustrate its implementation in robotic joints.

The main contribution of this work is the novel reconfigurable design of the compliant joint mechanism. The new compliant joint is able to change its stiffness from zero to a specified range, which is determined through design parameters and configurations. Moreover, the new joint can vary its stiffness in different modes including linear, hardening and softening modes. The three modes can be observed in all configurations by adjusting spring pretension. The joint shows hardening mode first with small spring pretension, then transits to linear mode and finally softening mode with the increase of spring pretension.

The novel revolute joint is able to achieve various stiffness performance and large range of stiffness variation. A potential application of JVSR is to be used as a passive compliant joint or to integrate into electric motors to build compliant actuators. The new compliant joint can find their applications in exoskeletons, rehabilitation robots and servicing robots. Moreover, it can be used in walking, hopping, and running robots where the energy storage capability is required to improve the efficiency. JVSR can also be applicable to new coupling device, which is very common in motion transmissions. For future work, implementation case of modular robot joint based on the proposed design will be exploited.

Acknowledgment

The research is in part supported by Innovation Fund Denmark through Grand Solutions project Exo-aider. The first author acknowledges the CSC scholarship for his study at Aalborg University, Denmark.

Supplementary material

Supplementary material associated with this article can be found, in the online version, at doi:[10.1016/j.mechmachtheory.2018.12.011](https://doi.org/10.1016/j.mechmachtheory.2018.12.011).

References

- [1] B. Vanderborght, A. Albu-Schaeffer, et al., Variable impedance actuators: a review, *Rob. Auton. Syst.* 61 (12) (2013) 1601–1614.
- [2] H. Vallery, J. Veneman, E. van Asseldonk, R. Ekkelenkamp, M. Buss, H. van Der Kooij, Compliant actuation of rehabilitation robots, *IEEE Rob. Autom. Mag.* 15 (3) (2008) 60–69.
- [3] N. Vitiello, T. Lenzi, S. Roccella, S.M.M.D. Rossi, E. Cattin, F. Giovacchini, F. Vecchi, M.C. Carrozza, NEUROExos: a powered elbow exoskeleton for physical rehabilitation, *IEEE Trans. Rob.* 29 (1) (2013) 220–235.
- [4] J.A. Blaya, H. Herr, Adaptive control of a variable-impedance ankle-foot orthosis to assist drop-foot gait, *IEEE Trans. Neural Syst. Rehabil. Eng.* 12 (1) (2004) 24–31.
- [5] J.F. Veneman, R. Ekkelenkamp, R. Kruidhof, F.C. van der Helm, H. van der Kooij, A series elastic- and Bowden-cable-based actuation system for use as torque actuator in exoskeleton-type robots, *Int. J. Rob. Res.* 25 (3) (2006) 261–281.
- [6] W.M. dos Santos, G.A. Caurin, A.A. Siqueira, Design and control of an active knee orthosis driven by a rotary series elastic actuator, *Control Eng. Pract.* 58 (2017) 307–318.
- [7] K. Kong, J. Bae, M. Tomizuka, Control of rotary series elastic actuator for ideal force-mode actuation in human–robot interaction applications, *IEEE/ASME Trans. Mechatron.* 14 (1) (2009) 105–118.
- [8] K. Kong, J. Bae, M. Tomizuka, A compact rotary series elastic actuator for human assistive systems, *IEEE/ASME Trans. Mechatron.* 17 (2) (2012) 288–297.
- [9] G. Chen, P. Qi, Z. Guo, H. Yu, Mechanical design and evaluation of a compact portable kneeanklefoot robot for gait rehabilitation, *Mech. Mach. Theory* 103 (2016) 51–64.

- [10] H.Q. Vu, X. Yu, F. Iida, R. Pfeifer, Improving energy efficiency of hopping locomotion by using a variable stiffness actuator, *IEEE/ASME Trans. Mechatron.* 21 (1) (2016) 472–486.
- [11] J.W. Hurst, A.A. Rizzi, Series compliance for an efficient running gait, *IEEE Rob. Autom. Mag.* 15 (3) (2008) 42–51.
- [12] R.V. Ham, B. Vanderborght, M.V. Damme, B. Verrelst, D. Lefever, MACCEPA, the mechanically adjustable compliance and controllable equilibrium position actuator: design and implementation in a biped robot, *Rob. Auton. Syst.* 55 (10) (2007) 761–768.
- [13] A. Albu-Schäffer, S. Haddadin, C. Ott, A. Stemmer, T. Wimbck, G. Hirzinger, The DLR lightweight robot: design and control concepts for robots in human environments, *Ind. Robot Int. J.* 34 (5) (2007) 376–385.
- [14] L. Zhou, S. Bai, Integrated dimensional and drive-train design optimization of a light-weight anthropomorphic arm, *Rob. Auton. Syst.* 60 (1) (2012) 113–122.
- [15] L. Zhou, S. Bai, A new approach to design of a lightweight anthropomorphic arm for service applications, *J. Mech. Robot* 7 (3) (2015) 031001.
- [16] T. Verstraten, J. Geeroms, G. Mathijssen, B. Convens, B. Vanderborght, D. Lefever, Optimizing the power and energy consumption of powered prosthetic ankles with series and parallel elasticity, *Mech. Mach. Theory* 116 (2017) 419–432.
- [17] T. Verstraten, P. Beckerle, R. Furnémont, G. Mathijssen, B. Vanderborght, D. Lefever, Series and parallel elastic actuation: impact of natural dynamics on power and energy consumption, *Mech. Mach. Theory* 102 (2016) 232–246.
- [18] S. Wolf, G. Grioli, et al., Variable stiffness actuators: review on design and components, *IEEE/ASME Trans. Mechatron.* 21 (5) (2016) 2418–2430.
- [19] J. Austin, A. Schepelman, H. Geyer, Control and evaluation of series elastic actuators with nonlinear rubber springs, in: Proceedings of the IEEE/RSJ International Conference on Intelligent Robots and Systems, 2015, pp. 6563–6568.
- [20] J.J. Park, Y.J. Lee, J.B. Song, H.S. Kim, Safe joint mechanism based on nonlinear stiffness for safe human-robot collision, in: Proceedings of the IEEE International Conference on Robotics and Automation, 2008, pp. 2177–2182.
- [21] S.A. Migliore, E.A. Brown, S.P. DeWeerth, Novel nonlinear elastic actuators for passively controlling robotic joint compliance, *J. Mech. Des.* 129 (4) (2007) 406–412.
- [22] T. Bacek, M. Moltedo, C. Rodriguez-Guerrero, J. Geeroms, B. Vanderborght, D. Lefever, Design and evaluation of a torque-controllable knee joint actuator with adjustable series compliance and parallel elasticity, *Mech. Mach. Theory* 130 (2018) 71–85.
- [23] S. Wolf, G. Hirzinger, A new variable stiffness design: matching requirements of the next robot generation, in: Proceedings of the IEEE International Conference on Robotics and Automation, 2008, pp. 1741–1746.
- [24] S. Groothuis, R. Carloni, S. Stramiglio, A novel variable stiffness mechanism capable of an infinite stiffness range and unlimited decoupled output motion, *Actuators* 3 (2) (2014) 107–123.
- [25] D. Hyun, H.S. Yang, J. Park, Y. Shim, Variable stiffness mechanism for human-friendly robots, *Mech. Mach. Theory* 45 (6) (2010) 880–897.
- [26] A. Jafari, N.G. Tsagarakis, D.G. Caldwell, AwAS-II: a new actuator with adjustable stiffness based on the novel principle of adaptable pivot point and variable lever ratio, *Proceedings of the IEEE International Conference on Robotics and Automation*, pp. 4638–4643.
- [27] A. Jafari, N.G. Tsagarakis, D.G. Caldwell, A novel intrinsically energy efficient actuator with adjustable stiffness (AwAS), *IEEE/ASME Trans. Mechatron.* 18 (1) (2013) 355–365.
- [28] L. Liu, S. Leonhardt, B.J. Misgeld, Design and control of a mechanical rotary variable impedance actuator, *Mechatronics* 39 (2016) 226–236.
- [29] H.V. Quy, L. Aryananda, F.I. Sheikh, F. Casanova, R. Pfeifer, A novel mechanism for varying stiffness via changing transmission angle, in: Proceedings of the IEEE International Conference on Robotics and Automation, 2011, pp. 5076–5081.
- [30] J. Choi, S. Hong, W. Lee, S. Kang, M. Kim, A robot joint with variable stiffness using leaf springs, *IEEE Trans. Rob.* 27 (2) (2011) 229–238.
- [31] X. Li, W. Chen, W. Lin, K.H. Low, A variable stiffness robotic gripper based on structure-controlled principle, *IEEE Trans. Autom. Sci. Eng.* 99 (2017) 1–10.
- [32] M.G. Catalano, G. Grioli, M. Garabini, F. Bonomo, M. Mancini, N. Tsagarakis, A. Bicchi, VSA-CubeBot: a modular variable stiffness platform for multiple degrees of freedom robots, in: Proceedings of the IEEE International Conference on Robotics and Automation, 2011, pp. 5090–5095.
- [33] N.G. Tsagarakis, I. Sardellitti, D.G. Caldwell, A new variable stiffness actuator (CompAct-VSA): design and modelling, in: Proceedings of the IEEE/RSJ International Conference on Intelligent Robots and Systems, 2011, pp. 378–383.
- [34] I. Thorson, D. Caldwell, A nonlinear series elastic actuator for highly dynamic motions, in: Proceedings of the IEEE/RSJ International Conference on Intelligent Robots and Systems, 2011, pp. 390–394.
- [35] M. Kilic, Y. Yazicioglu, D.F. Kurtulus, Synthesis of a torsional spring mechanism with mechanically adjustable stiffness using wrapping cams, *Mech. Mach. Theory* 57 (2012) 27–39.
- [36] B. Vanderborght, N.G. Tsagarakis, C. Semini, R.V. Ham, D.G. Caldwell, MACCEPA 2.0: adjustable compliant actuator with stiffening characteristic for energy efficient hopping, in: Proceedings of the IEEE International Conference on Robotics and Automation, 2009, pp. 544–549.
- [37] D. Owaki, A. Ishiguro, Enhancing stability of a passive dynamic running biped by exploiting a nonlinear spring, in: Proceedings of the IEEE/RSJ International Conference on Intelligent Robots and Systems, 2006, pp. 4923–4928.
- [38] S. Bai, S. Christensen, M.R.U. Islam, An upper-body exoskeleton with a novel shoulder mechanism for assistive applications, in: Proceedings of the IEEE International Conference on Advanced Intelligent Mechatronics, 2017, pp. 1041–1046.
- [39] S. Christensen, S. Bai, Kinematic analysis and design of a novel shoulder exoskeleton using a double parallelogram linkage, *J. Mech. Robot.* 10 (4) (2018) 041008.
- [40] J. Gere, *Mechanics of Materials*, Thomson Learning, United States of America, 2004.